Petroleum Science 23 (2026) 447–463

Contents lists available at ScienceDirect

Petroleum Science

journal homepage: www.keaipublishing.com/en/journals/petroleum-science

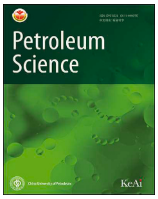

Original Paper

Particle dynamics and wear characteristics of lining layers in curved non-metallic flexible pipes for deep-sea mining

Ying-Ying Wang[a,*], Yun-Di Liu[b], Ze-Qing Lin[a], Hai-Bo Sun[a], Zhuo Cheng[c], Ke Wang[c], Ding-Wen Huang[a]

[a] Hainan Institute of China University of Petroleum (Beijing), Sanya, 572000, Hainan, China
[b] CNOOC China Limited, Hainan Branch, Haikou, 570312, Hainan, China
[c] College of Mechanical and Transportation Engineering, China University of Petroleum (Beijing), Beijing 102249, China

ARTICLE INFO

Article history:
Received 17 October 2024
Received in revised form
3 July 2025
Accepted 5 November 2025
Available online 12 November 2025

Edited by Teng Zhu

Keywords:
Deep-sea mining
Non-metallic flexible pipe
CFD-DEM simulation
Internal layer wear
Hydraulic lifting system
Particle dynamics

ABSTRACT

Wear of the internal lining in the non-metallic flexible pipes (NMFPs) is a critical issue in long-distance hydraulic lifting for deep-sea mining, as it can lead to structural failure and reduced service life. The non-homogeneous, discontinuous flow of unevenly sized mineral particles, especially in the curved sections of the pipe, complicates the analysis of particle motion and wear characteristics. This research presents a numerical simulation model of particle dynamics in the internal layers of curved NMFPs, developed using the CFD-DEM coupling method, based on Hertz-Mindlin contact theory and the Archard wear model. The model captures the particle-particle and particle-wall collision behaviors, alongside energy dissipation patterns. A parametric analysis of the wear process was conducted to evaluate the service life of the bent NMFP. Results indicate that particle collision frequency and energy dissipation correlate with increased wear, while higher conveying speeds and larger particle diameters intensify wear. Under specified conditions of 6 m/s conveying speed and a maximum particle concentration of 0.15, an NMFP with a 10 mm internal layer thickness is estimated to last 3.65 years. These findings provide a technical reference for optimizing conveying parameters and minimizing internal wear in deep-sea hydraulic lifting systems at depths of 6000 m.

Nomenclature

v	Fluid velocity, m/s (Eq. (1))
t	Time, s
ρ_f	Fluid density, s
p	Pressure, Pa
η	Fluid kinematic viscosity, kg/m^3
f_g	Fluid gravity, N
Q	The volume of liner material removed, m^3 (Eq. (3))
P_c	Contact surface normal pressure, N
L_c	Distance of tangential relative sliding of mineral particles along the wall, m
H	Softest surface Brinell hardness of the material being worn, Pa
K	An empirical constant characterizing the relationship between the wear volume and all influencing factors except contact line normal stress, relative sliding speed, and material hardness

---

* Corresponding author.
E-mail address: wyy@cup.edu.cn (Y.-Y. Wang).
Peer review under the responsibility of China University of Petroleum (Beijing).

https://doi.org/10.1016/j.petsci.2025.11.015
1995-8226/

H_{p}	The wear depth of each cell, m (Eq. (4))
a	The contact area between the particles and the wall of the internal layer interior, m^2
u	The instantaneous velocity of the fluid, m/s (Eq. (5))
$\bar{\tau}$	Stress tensor, kg/m·s^2
f_{m}	Momentum exchange loss between the solid and liquid phases, (kg·m)/s
m_i	Mass of particle i, kg (Eq. (7))
v_i	The velocity of particle i, m/s
g	Gravitational acceleration, 9.8 m/s^2
F_{ci}	Contact force on particle i by all particles in contact, N
I_i	Particle rotation inertia, kg·m^2
ω_i	The angular velocity of particle i, rad/s
M_{ci}	Contact torque, N·m
M_{fi}	Fluid-induced torque, N·m
F_{t}	Tangential force, N
F_{n}	Normal force, N
F_{ci}	The vector sum of the normal and tangential contact forces, N
θ	Normal overlap, m
A_i	Particle radius, m
r_i	Position vectors of the spherical center of spherical particles i (Eq. (10))
R_{eq}	Equivalent radius of particles, m
r_{c}	Contact radius, m
E_{eq}	Equivalent elastic modulus (Eq. (12))
υ_i	Poisson ratios of particles
E_i	Elastic modulus of particles
F_{nd}	Normal damping force, N·m, (Eq. (14))
m_{eq}	Equivalent mass, kg
v_{ia}	Velocity before particle i collision, m/s
v_{nr}	Normal component value of the relative velocity, m/s
S_{n}	Normal stiffness
S_{t}	Tangential stiffness (Eq. (19))
ζ	Tangential overlap, m
F_{st}	Particle surface tension, N
G_{eq}	Equivalent shear modulus
F_{td}	Tangential damping force, N (Eq. (23))
v_{tr}	Value of the tangential component of the relative velocity, m/s

1. Introduction

Due to challenges like poor system stability, low mining efficiency, and significant seabed environmental impact, traditional methods such as the submarine drag bucket, continuous line bucket, and shuttle vessel have been phased out in favor of deep-sea polymetallic mining systems (Glasby et al., 2015; Hannington et al., 2017). The hydraulic lifting mining system (HLMS) has become widely adopted, successfully validated in sea trials by organizations such as OMA, OMI, GSR, and CRIMM. Compared to traditional rigid pipes, the non-metallic flexible pipe (NMFP) offers advantages like lighter weight, improved wear resistance, and easier retrieval, making it better suited for transporting mineral particles in a 6000-meter ultra-deep-sea manganese nodule HLMS (Leng et al., 2021) (Fig. 1).

The NMFP must endure external forces, such as waves and currents, as well as internal pressure from mineral-laden seawater. Its dynamic response to internal and external flows increases the complexity of the solid-liquid two-phase flow during the hydraulic lifting process. Mineral particles within the pipe are constantly influenced by drag force, pressure gradient force, and lift force. Continuous collisions between particles and with the inner wall of the NMFP can disturb the flow. Especially, with the increase of the particle size and quantity, it will lead to the formation of aggregates. These collisions also cause wear, particularly in curved sections, reducing the wall thickness of the pipe. A detailed analysis of the solid-liquid flow mechanism, particle velocity, and wear distribution is critical to minimizing blockage and internal wear, providing guidance for NMFP design and operational parameters.

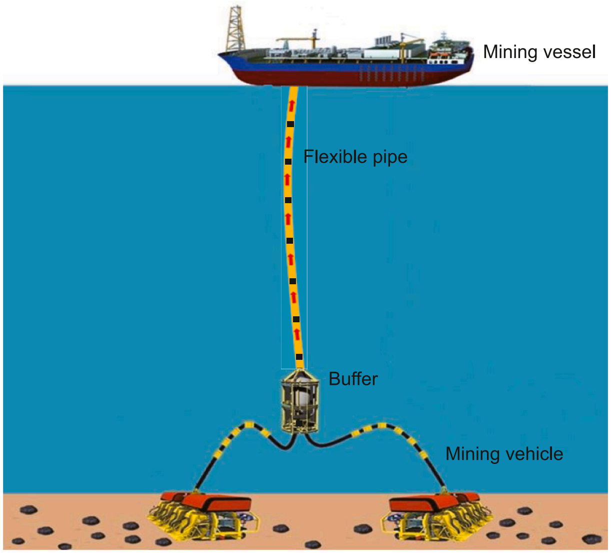

Fig. 1. The NMFP deep-sea HLMS.

Recent studies have extensively examined particle motion in gas-solid and solid-liquid mixtures in pipelines. Ran (Ran et al., 2006) developed a 3D model for gas-solid rotary flow using the Lagrangian method, while Chen (Chen et al., 2006) explored erosion in tees and elbows during gas-solid two-phase flow, validating results through experiments. Lu (Lu et al., 2009) extended Laser Doppler Anemometry to measure particle velocity in dilute pneumatic systems, and Yan (Yan et al., 2021) analyzed particle motion in bends with varying curvatures. Chen (Chen et al., 2010) studied slip flow in coal-water slurries in pipes of different diameters, while Choi (Choi et al., 2010, 2013) and Yang (Yang et al., 2015) investigated flow and drag behavior around free-falling particles. Van Wijk (Van Wijk et al., 2016) described transport processes using fluidization theory, and Chen (Chen et al., 2017) simulated Brownian motion of particles using the lattice Boltzmann model. Further, Liu (Liu et al., 2018) examined particle motion in impinging stream reactors, and Zhao (Zhao et al., 2020) studied erosion behavior in 304 stainless steel via liquid-solid two-phase jets.

In terms of wear models, Blanchard (Blanchard et al., 1984) tracked particle trajectories in erosion wear within a 90° bend, while Bellman (Bellman et al., 1981) identified debris formation from surface layers as a key factor in wear. Frawley (Frawley et al., 2009) introduced an erosion prediction model to reduce deviations in friction drag loss, with Wu (Wu et al., 2012) improving prediction accuracy through machine learning. Van Wijk (Van Wijk et al., 2014) and Zhang (Zhang et al., 2015) developed models accounting for particle size and sand dispersion, respectively. Shen (Shen et al., 2016) and Araoye (Araoye et al., 2017)

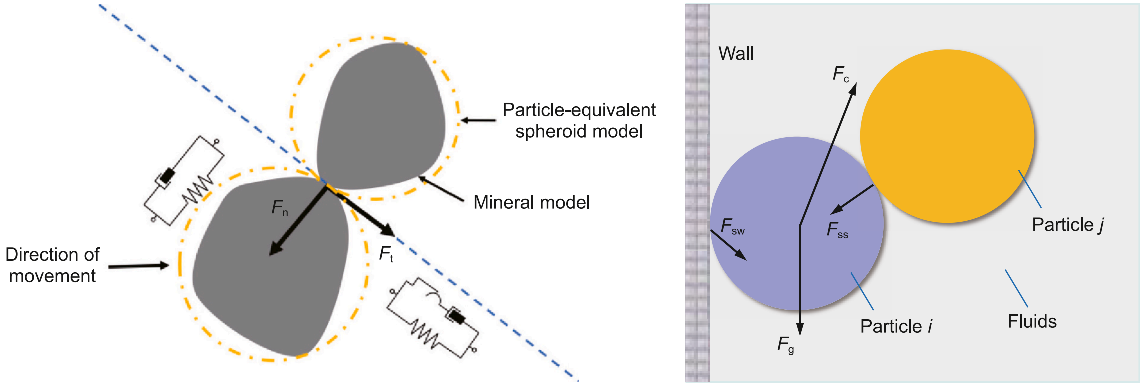

(a) Hertz-Mindlin contact model **(b)** Particle force model

Fig. 2. Particle collision model (Wang et al., 2024).

analyzed erosion in different particle and flow conditions, while Singh and Li (Singh et al., 2019; Li et al., 2021) studied erosion wear in slurry pipelines and bent pipes. Darihaki (Darihaki et al., 2021) and Takano (Takano et al., 2022) proposed and validated wear models for particle impacts. Liu, Yao and Wang (Liu et al., 2022; Yao et al., 2023; Wang et al., 2024) focused on wear due to particle shape, curvature, and two-phase flow dynamics.

Despite extensive research on particle parameters in pipeline transportation, studies on the mixed transport of large particles during solid-liquid two-phase flow in NMFPs are limited. Traditional erosion wear models struggle with large particle abrasion, especially in deep-sea HLMSs. Additionally, single-phase fluid-solid coupling models often overlook particle perturbation effects, leading to inaccurate simulations due to collisions and energy losses. Key factors such as NMFP size, mobility, and particle gradation must be considered when determining particle scale in deep-sea mining. Further investigation is needed into how particle gradation, two-phase concentration, and fluid velocity affect particle movement.

This paper uses the CFD-DEM coupling method to model particle movement and wall wear in the internal layer of a bent NMFP during deep-sea mining. The model evaluates particle collisions and energy changes to assess the service life of the NMFP. Results provide insights into mineral particle behavior under different transport conditions, informing NMFP structural design.

2. Modeling methods

Numerical simulation requires fundamental fluid mechanics and particle collision theories, including governing equations for discrete and continuous phases, and analysis of forces acting on particles in the flow field.

2.1. Governing equations

In deep-sea mining, the solid-liquid two-phase flow treats seawater as the continuous phase and mineral particles as the discrete phase. The fluid motion in the continuous phase is described by the Navier-Stokes (N-S) equations (Badur et al., 2011), which model momentum conservation in viscous incompressible fluids and include mass, momentum, and energy conservation laws. For seawater, the conservation of mass and momentum form a closed set of equations. The mass conservation equation (Eq. (1)) represents the continuity equation, dealing with mass inflow, outflow, and changes in density over time within a closed system. The momentum conservation equation (Eq. (2)) follows Newton's second law, where the change in fluid momentum equals the sum of external forces:

$$\nabla \cdot v = 0 \tag{1}$$

$$\frac{\partial v}{\partial t} + v \cdot \nabla v = -\frac{1}{\rho_{\mathrm{f}}}\nabla p + \eta \cdot \nabla^2 v + f_{\mathrm{g}} \tag{2}$$

The Archard model, which is widely applied in the field of wear research, indicates that the amount of wear loss from the inner surface of a material is proportional to the corresponding frictional wear caused by the movement of particles, as presented in Eq. (3):

$$Q = K\frac{P_{\mathrm{c}} L_{\mathrm{c}}}{H} \tag{3}$$

where Q is the volume of liner material removed, P_{c} is the contact surface normal pressure, L_{c} is the distance of tangential relative sliding of mineral particles along the wall, H is the softest surface Brinell hardness of the material being worn, K is the empirical constant characterizing the relationship between the wear volume and all influencing factors except contact line normal stress.

The Brinell hardness of the material surface, the tangential relative slip distance, and the normal pressure on the contact surface represent the main parameters influencing the degree of wear in the Archard model. Other factors influencing the amount of wear are considered in K, which must be measured via tests and vary according to different contact environment. The equation for the wear depth of each cell in the discrete phase within the EDEM is expressed in Eq. (4):

$$H_{\mathrm{p}} = \frac{Q}{a} \tag{4}$$

where H_{p} is the wear depth of each cell, a is the contact area between the particles and the wall of the internal layer interior.

The Euler-Lagrange method considers the volume fraction of mineral particles. It is used to establish the continuous-phase and discrete-phase control equations by taking into account the two-way coupling of particle-particle and particle-wall interactions.

2.2. Continuous-phase control equations

This study uses the RNG k-ε turbulence model in the Eulerian coordinate system to solve and analyze the flow field in the NMFP. All continuous phases are numerically calculated in absolute coordinates, as shown in Eq. (5) (Lin et al., 2024):

$$\frac{\partial \rho_f}{\partial t} + \nabla\left(\rho_f u\right) = 0 \quad (5)$$

where u is the instantaneous velocity of the fluid.

Eq. (6) expresses momentum conservation:

$$\frac{\partial}{\partial t}\left(\rho_f u\right) + \nabla\left(\rho_f u\right) = -\nabla p + \nabla(\overline{\tau}) + \rho_f g + f_m \quad (6)$$

where $\overline{\tau}$ is the stress tensor, f_m is the momentum exchange loss between the solid and liquid phases.

In deep-sea mining, the mineral particles that are transported during NMFP hydraulic lifting are treated as discrete phases. Discrete phase particle control is solved using Newton's second law to calculate the interaction between the fluid. The particles and the flow field are solved using the N-S equation, as expressed in Eqs. (7) and (8):

$$m_i \frac{\mathrm{d}v_i}{\mathrm{d}t} = m_i g + F_{mi} + F_{ci} \quad (7)$$

$$I_i \frac{\mathrm{d}\omega_i}{\mathrm{d}t} = M_{ci} + M_{fi} \quad (8)$$

where m_i is mass of particle i, v_i is the velocity of particle i, g is the acceleration of gravity, F_{ci} is the contact force on particle i by all particles in contact, I_i is the particle rotation inertia, ω_i is the angular velocity of particle i, M_{ci} is the contact torque, M_{fi} is the fluid-induced torque.

2.3. The Hertz-Mindlin no-sliding contact model

Fluid drag force, fluid lift force, pressure gradient force, and added mass force are considered in this paper. As shown in Fig. 2, based on the Hertz-Mindlin contact theory model without sliding, the normal contact force and tangential contact force generated during the particle collision process are described.

The contact force generated by the collision of particles in contact includes the normal force F_n and tangential force F_t. The resultant force F_{ci} is the vector sum of two normal contact forces and tangential contact forces. The calculation of the normal force in the Hertz-Mindlin model is grounded in the Hertz contact model. It is necessary to assume that the contact surface between particles is smooth, the area of the contact surface is much smaller than the surface area of the particles, and that only elastic deformation occurs during particle contact.

2.3.1. Normal force in particle collision

The normal force was calculated based on the Mindlin model, Hertz-Mindlin is shown in Eq. (9):

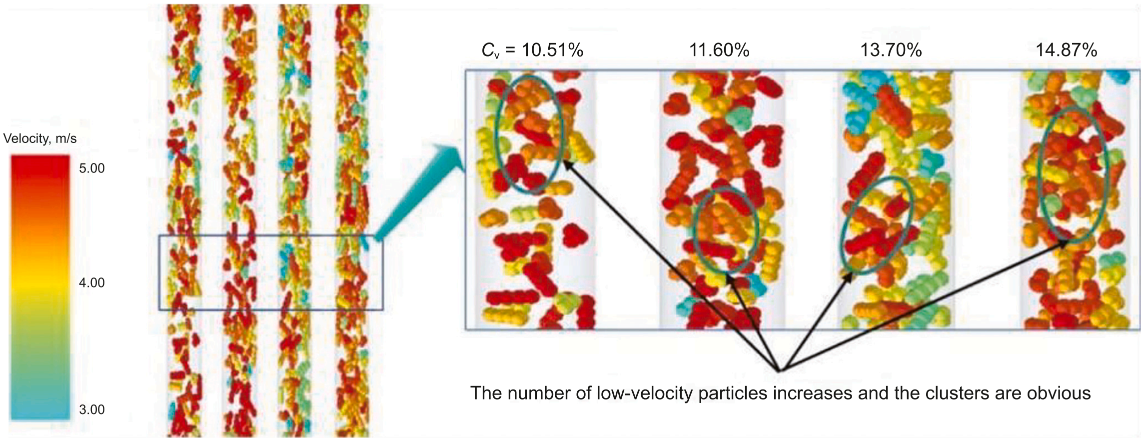

Fig. 3. Transport characteristics of heterogeneous particles (Wang et al., 2024).

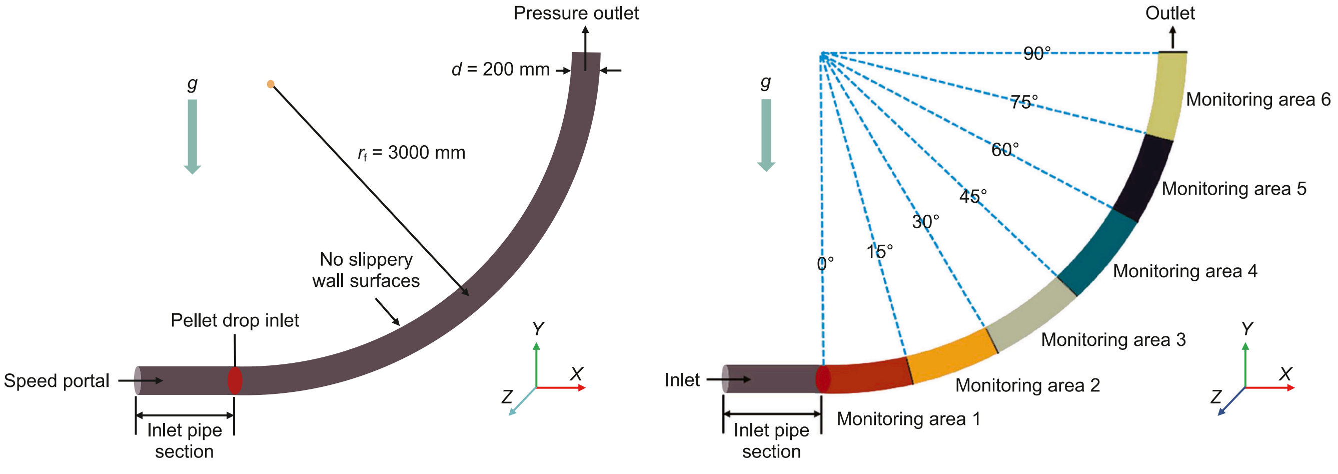

(a) Computational domain model **(b)** Monitoring area locations

Fig. 4. The calculation domain model of a bent NMFP.

Table 1
Model parameters.

Parameter names	Value	Parameter names	Value
Outlet pressure	0 MPa	Pipe diameter	200 mm
Normal wall velocity	0 m/s	Particle diameter	20 mm
Tangential wall velocity	0 m/s	Bending radius	4 m
Particle concentration	2000 kg/m^3	Gravity acceleration	9.81 m/s^2
Transfer rate	3 m/s		

$$F_{ci} = F_n + F_t \tag{9}$$

The normal overlap θ of elastic contact between two spherical particles with radius A_i and A_j is shown in Eq. (10), the contact surface of particles i and j is circular, and the contact radius r_c is shown in Eq. (11):

$$\theta = A_i + A_j - |r_i - r_j| \tag{10}$$

$$r_c = \sqrt{\theta R_{eq}} \tag{11}$$

where r_i and r_j are the position vectors of the spherical center of spherical particles i and j; R_{eq} is the equivalent radius of particles, m.

The normal force F_n of the particle is shown in Eq. (12) (Yin et al., 2025):

$$F_n = \frac{4}{3}E_{eq}(R_{eq})^{\frac{1}{2}}\theta^{\frac{3}{2}} \tag{12}$$

$$E_{eq} = \frac{1-\upsilon_i}{E_i} + \frac{1-\upsilon_j}{E_j} \tag{13}$$

where E_{eq} is the equivalent elastic modulus; υ_i and υ_j are the poisson ratios of particles i and j; and E_i and E_j are the elastic modulus of particles i and j. The normal damping force F_{nd} is shown in Eq. (14):

$$F_{nd} = -2\sqrt{\frac{5}{6}}\frac{\ln e}{\sqrt{\ln^2 e + \pi^2}}\sqrt{S_n m_{eq}}\upsilon_{nr} \tag{14}$$

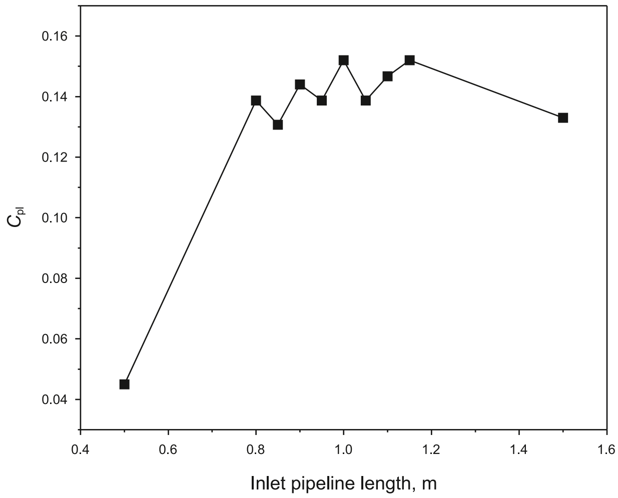

Fig. 5. Analysis of inlet pipeline length.

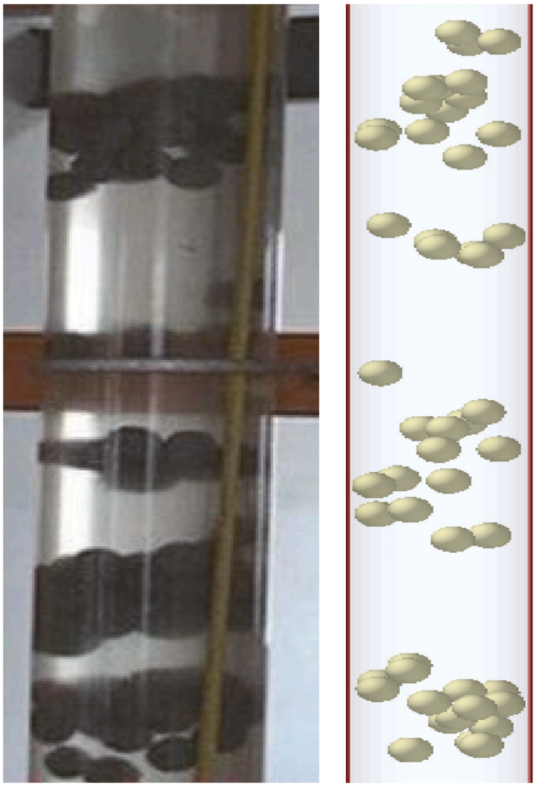

Fig. 6. Result comparisons between numerical simulation and experimental (Yang et al., 2011).

$$m_{eq} = \frac{m_i m_j}{m_i + m_j} \tag{15}$$

$$n = \frac{r_i - r_j}{|r_i - r_j|} \tag{16}$$

$$\upsilon_{nr} = \left(\upsilon_{ia} - \upsilon_{ja}\right)n \tag{17}$$

$$S_n = 2E_{eq}\sqrt{R_{eq}\theta} \tag{18}$$

where m_{eq} is the equivalent mass, kg; v_{ia} is the velocity before particle i collision, m/s; v_{ja} is the velocity before particle j collision, m/s; n is the normal unit vector during the collision; v_{nr} is the normal component value of the relative velocity; S_n is the normal stiffness, and e is the recovery coefficient.

2.3.2. Tangential force in particle collision

The tangential force F_t of the particle is shown in Eq. (19):

$$F_t = -S_t\zeta \tag{19}$$

$$S_t = 8G_{eq}\sqrt{R_{eq}\zeta} \tag{20}$$

$$\zeta = \frac{\theta^2}{R_{eq}} - \sqrt{\frac{4\pi\theta F_{st}}{E_{eq}}} \tag{21}$$

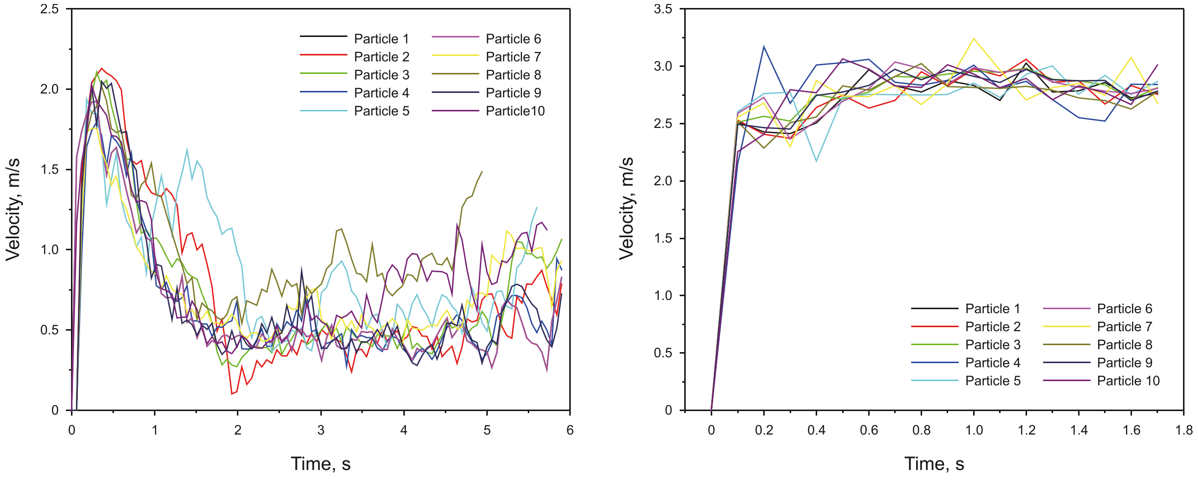

(a) u_f = 2 m/s

(b) u_f = 3 m/s

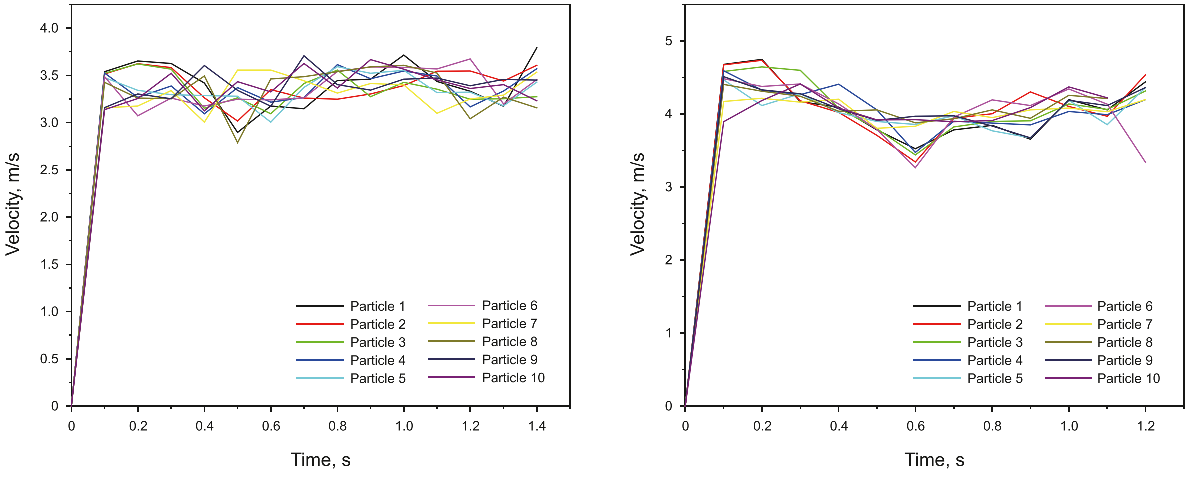

(c) u_f = 4 m/s

(d) u_f = 5 m/s

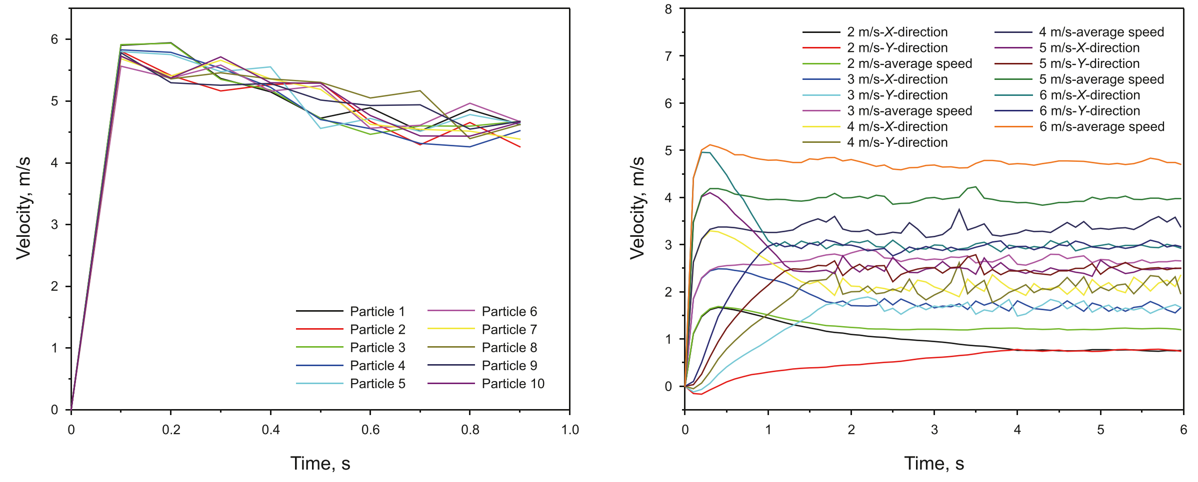

(e) u_f = 6 m/s

(f) An average particle velocity comparison at different conveying speeds

Fig. 7. The time history of the particle velocity at different conveying speeds.

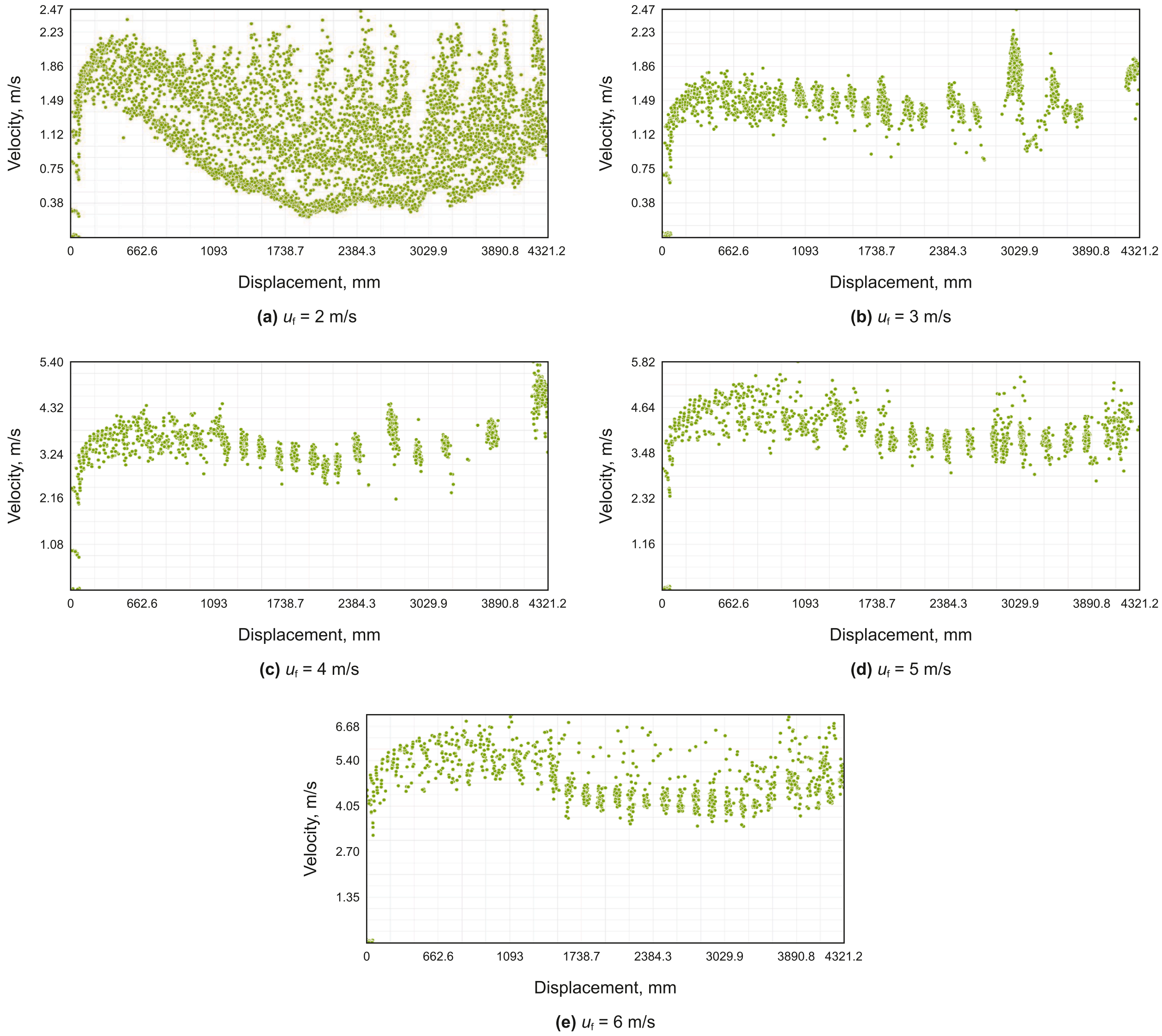

(a) u_f = 2 m/s

(b) u_f = 3 m/s

(c) u_f = 4 m/s

(d) u_f = 5 m/s

(e) u_f = 6 m/s

Fig. 8. The particle displacement-velocity scatter plot.

$$G_{\text{eq}} = \frac{2(2-\upsilon_i)(1+\upsilon_i)}{E_i} - \frac{2\left(2-\upsilon_j\right)\left(1+\upsilon_j\right)}{E_j} \tag{22}$$

where S_t is the tangential stiffness; ζ is the tangential overlap, m; F_{st} is the particle surface tension, N; G_{eq} is the equivalent shear modulus. The tangential damping force F_{td} is shown in Eq. (23):

$$F_{\text{td}} = -2\sqrt{\frac{5}{6}}\frac{\ln e}{\sqrt{\ln^2 e + \pi^2}}\sqrt{S_t m_{\text{eq}}}v_{\text{tr}} \tag{23}$$

$$v_{\text{tr}} = \left(v_i - v_j\right)t \tag{24}$$

where v_{tr} is the value of the tangential component of the relative velocity; t is the unit vector of the tangents at the time of the collision.

2.4. Deep sea mining hydraulic lift modeling

Ores exhibit diverse morphologies. Nevertheless, during the long-distance hydraulic transportation of ores, the shear force induced by collisions among particles and other factors will further facilitate the spheroidization of particles. The spheroidized particle model is more in line with the actual engineering situation. Meanwhile, in existing research, for particles with irregular shapes, the quasi-spherical simulation method is mainly employed to enhance the computational efficiency. This study adopted a spherical assumption based on the fact that after crushing and grinding, 85% of the particles in seabed ores have an aspect ratio <1.5 (as cited in “Guidelines for Deep Sea Mineral Processing Technology”), and shear forces during hydraulic conveying further promote sphericity (electron microscope observations show a sphericity >0.7). It can be seen that the assumption in this paper that the particles are quasi-spherical is highly consistent with the engineering reality. In fact, additional studies on the impact of anisotropic particles on hydraulic conveying have been thoroughly considered in published articles (Wang et al., 2024), as shown in Fig. 3. Spherical particles ensure stable and efficient transport with minimal loss and blockage, whereas mixed gradations with special-shaped particles exhibit significant fluctuations and reduced transport efficiency. Thus, spherical particles have advantages in improving conveying efficiency and avoiding pipe blockages. In fact, in the deep-sea mining

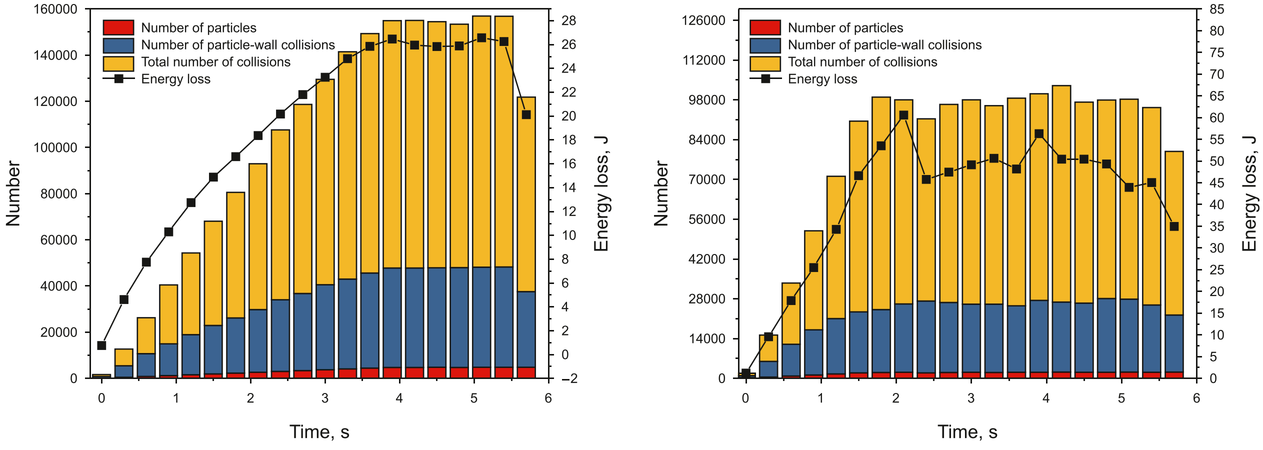

(a) u_f = 2 m/s **(b)** u_f = 3 m/s

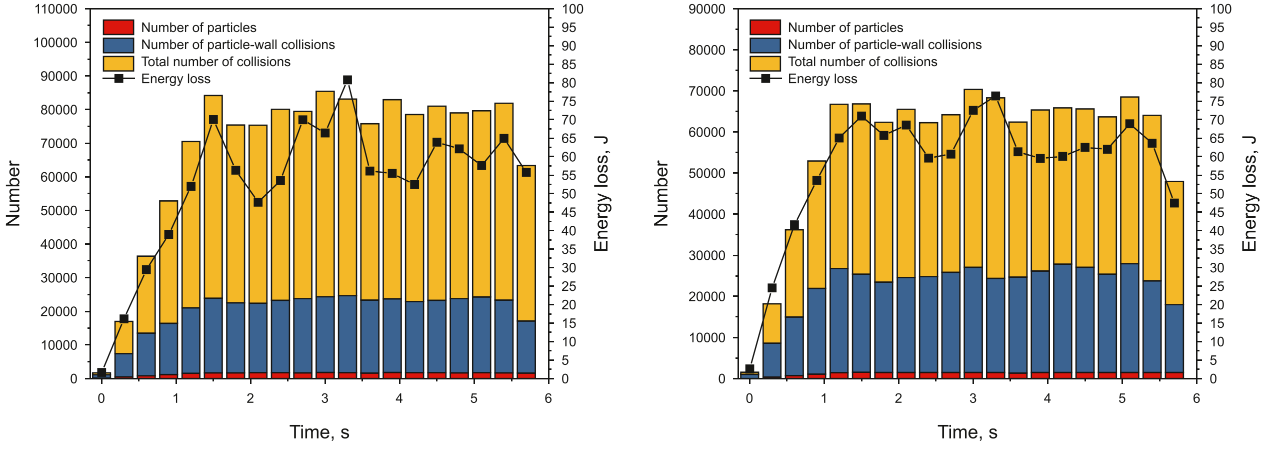

(c) u_f = 4 m/s **(d)** u_f = 5 m/s

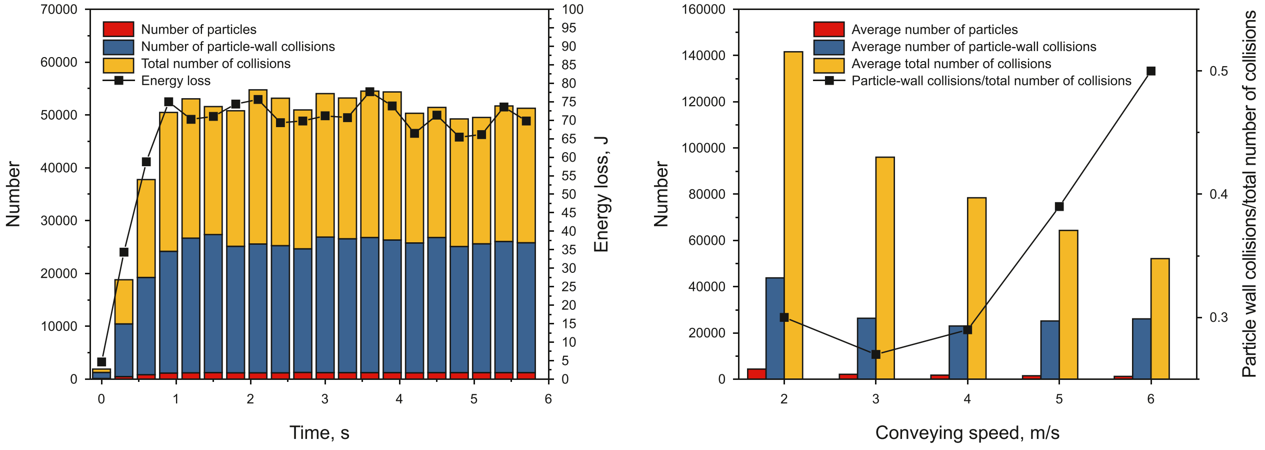

(e) u_f = 6 m/s **(f)** Particle collision analysis in a stable flow field

Fig. 9. Particle collision analysis at different conveying speeds.

process, the ore particles collected on the seabed are crushed to a spherical shape before being transported through pipes. Therefore, only the shapes of anisotropic particles are assumed in this paper.

Fig. 4 shows the bent NMFP calculation domain model, while Table 1 presents the model parameters. The skeleton layer determines the ultimate bending radius of the flexible pipe. During deep-sea mining operations at depths of 6000 m, the top end of the flexible pipe is subjected to significant axial tension. The skeleton layer must resist the internal compressive force generated by the tensile reinforcement layer. Therefore, while ensuring the skeleton layer can withstand the internal compressive force, it is designed in accordance with actual engineering parameters. Additionally, considering the installation and storage radius of the subsequent flexible pipe and the actual conditions of the reel, the

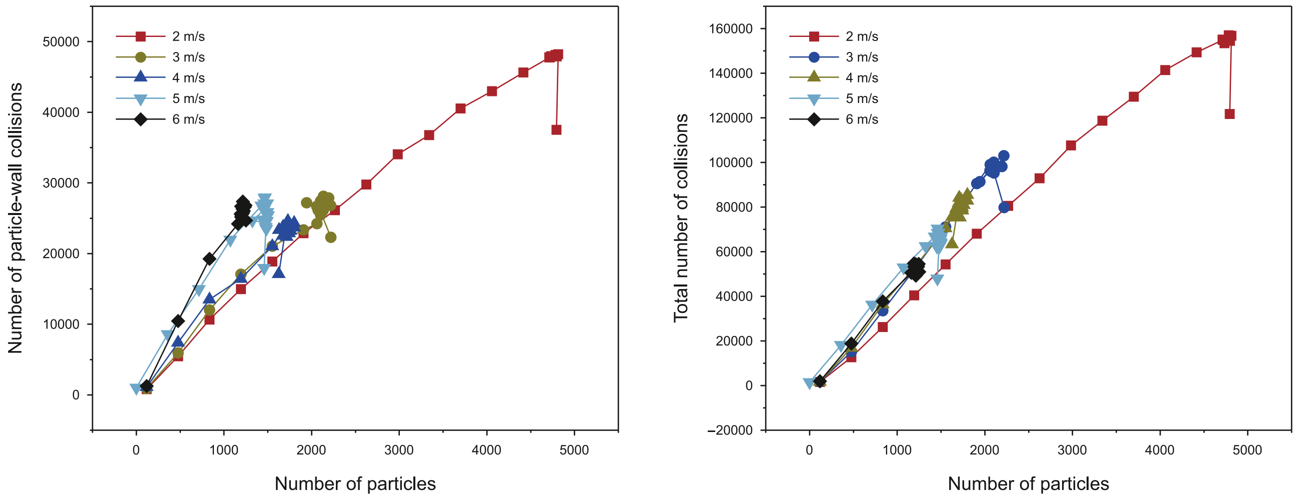

(a) Number of particle-to-wall collisions

(b) Total number of collisions

Fig. 10. Particle count-number of collisions curve.

ultimate bending radius of the flexible pipe is set at 4 m (Sun et al., 2024, 2026).

The number of points in the flow field determined the accuracy of the average value. To increase the local velocity accuracy of the flow field in the monitoring zone, the number of flow field monitoring points had to be maximized. The subsequent monitoring zone was divided as shown in Fig. 4. In terms of spatial distribution, six monitoring zones were established at 0°–15°, 15°–30°, 30°–45°, 45°–60°, 60°–75°, and 75°–90° of the bent NMFP.

In order to fully develop the turbulence flow into the vertical pipe to form a stable flow, as well as to eliminate the influence of the outlet reflux on the fluid in the pipe, a certain section of the inlet pipe needs to be added at the front end of the flexible pipe. In the process of CFD-DEM coupling, the computational workload is substantial, and the calculation time will increase significantly. As shown in Fig. 5, when the inlet length is 1 m, the local concentration of the particles C_{pl} is stable at about 0.15, with a small variation. Therefore, it can be considered that when the calculated domain length is 1 m, the solid-liquid two-phase flow in the pipeline reaches a stable state.

The accuracy of the numerical simulation of solid-liquid two-phase flow within a vertical pipe has been validated by comparing it with existing experimental data. The experimental images are from references (Yang et al., 2011), as shown in Fig. 6. The particle diameter is 45–50 mm, the average wet density is 2000 kg/m^3, and the inner diameter of the pipe is 200 mm. In the numerical simulation, the diameter of the selected particles is 50 mm, the average wet density is 2000 kg/m^3, and the inner diameter of the pipe is 200 mm. From the results of experiments and numerical simulations, it can be seen that when large-size uniform particles are hydraulically transported in the straight pipe section, due to the collision and extrusion between particles, they tend to gather together and form stratification. Numerical simulations accurately represent the aggregation of particles to form particle clusters.

3. Results and discusstion

3.1. Particle velocity

Generally, the minimum hydraulic conveying speed of a pipe should be 3 to 5 times the particle settling velocity, with a minimum speed of 3.6 m/s. This paper focuses on the engineering mining requirements where the pulp concentration is 15% and the flow rate exceeds 400 m^3/h. To meet future commercial mining needs, pipes with diameters over 200 mm are required. Therefore, in this paper, five conveying speeds of 2, 3, 4, 5 and 6 m/s are considered. Ten particles were randomly selected at the particle drop inlet and tracked as soon as they entered the flow field. Fig. 7 illustrates particle velocity in the flow field over time at different conveying speeds. Upon entering the flow field, particle velocity rose sharply due to the motion of the conveying fluid. As transport progressed, particle velocity fluctuated around an average value, with some particles exiting the calculation domain prematurely due to high speed, causing an incomplete velocity curve. At a conveying velocity of 2 m/s, particle velocity initially spiked before declining. Velocity fluctuations occurred across all conveying speeds, and low speeds led to increased local particle concentration, causing limited accumulation. The average particle velocity at 2 m/s was 0.575 m/s, significantly lower than the conveying speed. After stabilization, the average velocities were 2.77, 3.37, 4.07, and 4.96 m/s at conveying speeds of 3, 4, 5, and 6 m/s, respectively. As shown in Fig. 7(f), higher conveying speeds led to greater average particle velocities upon stabilization. Additionally, the time required for the *Y*-direction velocity to stabilize decreased with increased conveying velocity, while the *X*-direction velocity initially surged as particles entered the flow field, before gradually stabilizing.

Fig. 8 presents a scatter diagram of particle displacement-velocity distribution at conveying speeds ranging from 2 m/s to 6 m/s, with each dot representing a particle. At all speeds, particle velocity increased sharply as the flow field stabilized. Over time, as more particles entered the flow field, their velocities decreased, leading to a more uniform velocity distribution. As conveying speed increased, noticeable particle aggregation occurred. At 2 m/s, the highest number of particles was observed in the flow field due to poor particle flow.

3.2. Particle collision

Mineral particles with diameters of 20 mm were employed for collision analysis. The feed concentration was standardized at 10 kg/s, while the conveying speed was varied. The tests included both particle-particle and particle-wall collisions. The total number of collisions exhibited a dependence on the conveying speed,

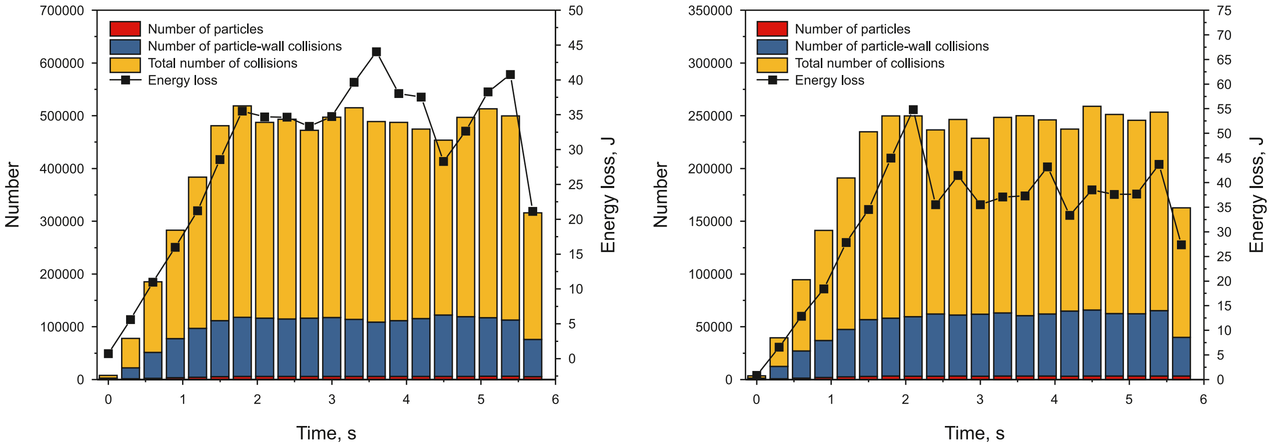

(a) d_p = 10 mm **(b)** d_p = 15 mm

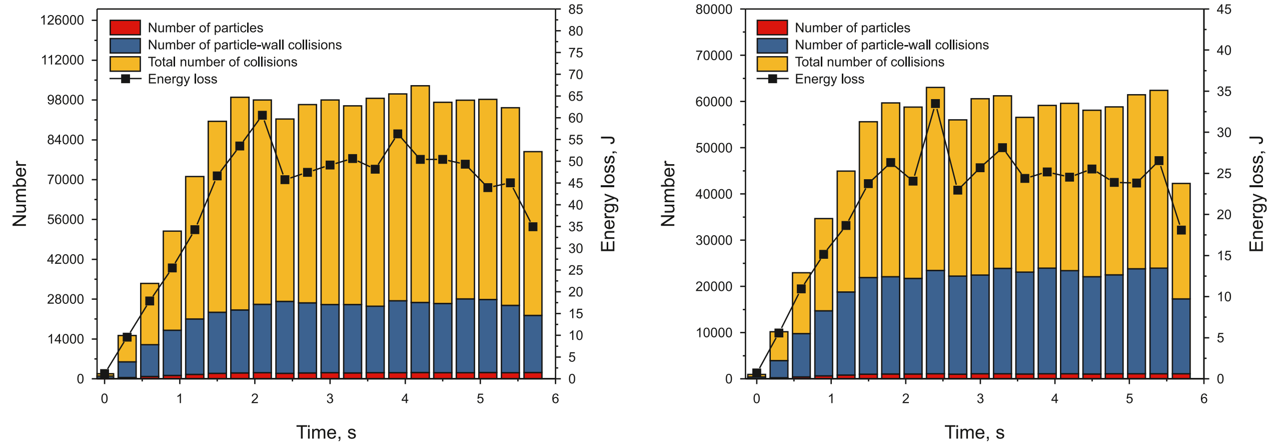

(c) d_p = 20 mm **(d)** d_p = 25 mm

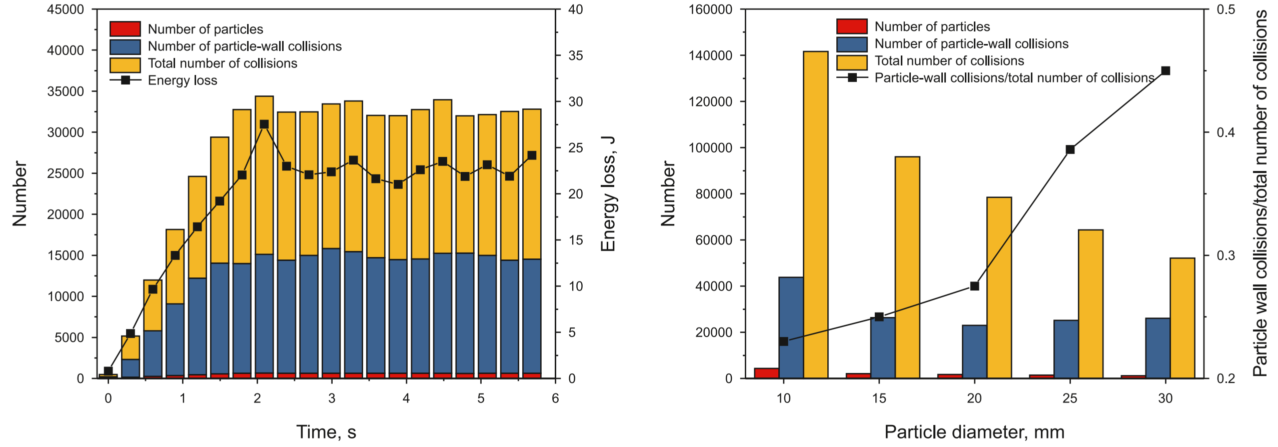

(e) d_p = 30 mm **(f)** Particle collision analysis in a stable flow field

Fig. 11. The collision analysis of particles with different diameters.

as illustrated in Fig. 9(a)–(e). Although the initial particle quantity was low, the number of collisions increased significantly as more particles entered the flow field. After a certain period, the fluid dynamics within the flow field and the total number of particle collisions reached a state of stabilization. This total number of collisions was associated with energy loss, demonstrating a consistent overall pattern and reflecting the stability of the flow field throughout the flexural pipe.

As the conveying speed increased, the time required for the computational domain to achieve stability decreased. The stable times recorded were 3.6, 1.8, 1.5, 1.3, and 1 s at conveying speeds of 2, 3, 4, 5, and 6 m/s, respectively. Notably, at conveying speeds

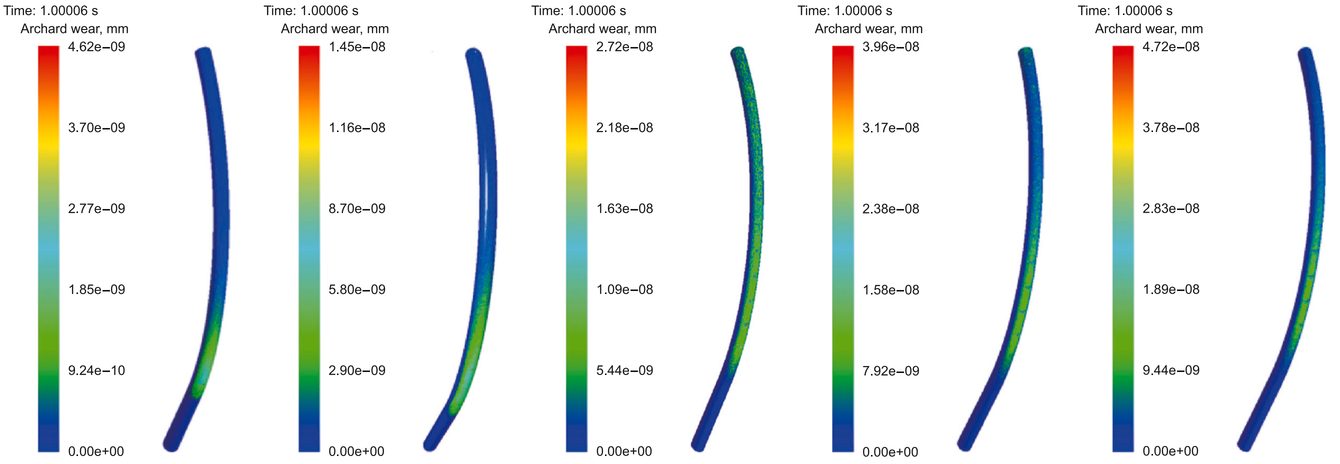

(a) u_f = 2 m/s **(b)** u_f = 3 m/s **(c)** u_f = 4 m/s **(d)** u_f = 5 m/s **(e)** u_f = 6 m/s

Fig. 12. The wear cloud of the NMFP interior at five transport speeds.

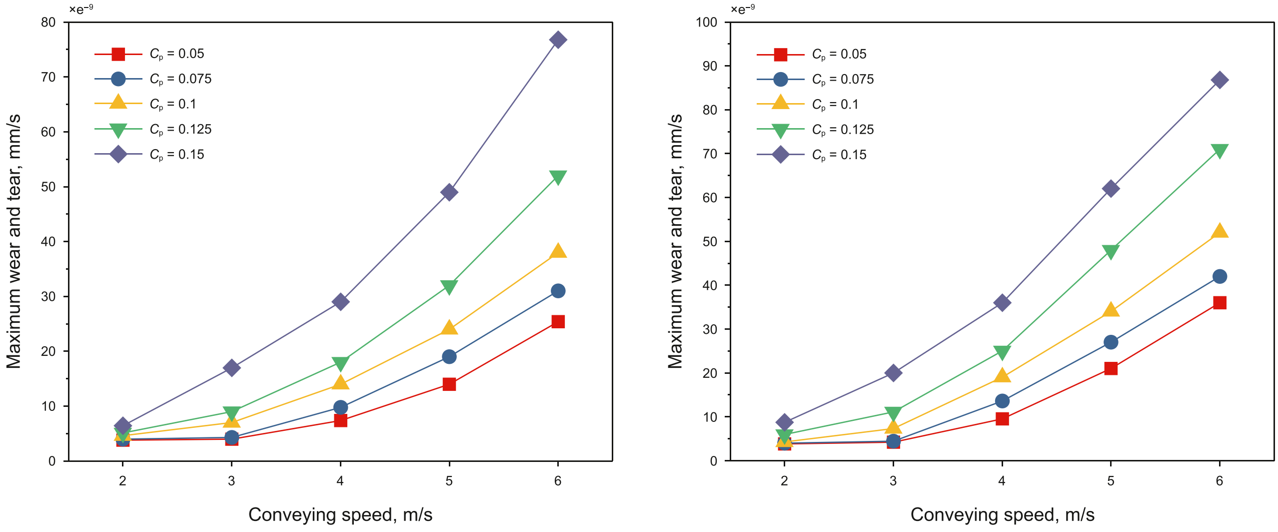

(a) Particle diameter of 20 mm **(b)** Particle diameter of 30 mm

Fig. 13. The maximum wear of the NMFP interior at different conveying speeds.

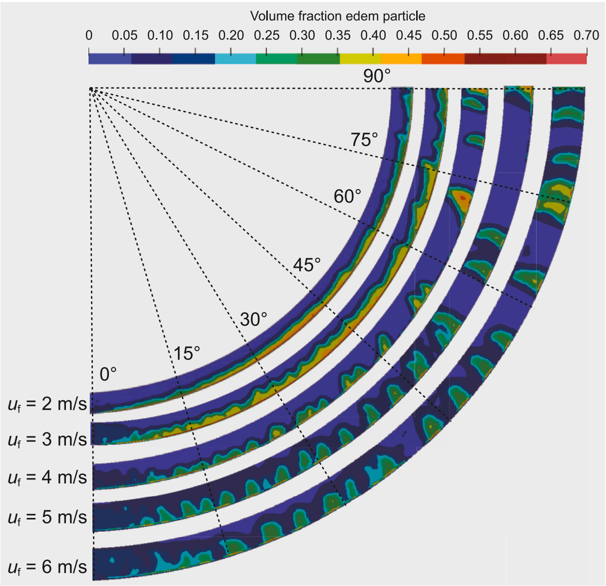

Fig. 14. The particle volume fraction distribution in the flow field at different conveying speeds.

exceeding 3 m/s, a positive correlation emerged between the number of collisions and the number of particles, indicating an increasing ratio between these two variables as particle quantity rose (Fig. 9(f)). Furthermore, the conveying velocity significantly influenced the proportion of particle-wall collisions relative to the total number of collisions, reaching 50% at a conveying speed of 6 m/s.

It can be seen from Fig. 10 that the number of particle-wall collisions and the total number of particle collisions are positively correlated with the increase in the number of particles.

When the particle diameters were varied while the conveying speed was kept at a constant value of 3 m/s and the feed concentration was maintained at 10 kg/s, the total number of collisions fluctuated within a period of 6 s (Fig. 11(a)–(e)). During this process, the time required for all collisions to stabilize was approximately 1.8 s. Energy loss was found to correlate with both particle diameters and the number of collisions. At a constant feed concentration, the number of particles in the flow field decreased as their diameters increased (Fig. 11(f)). When the flow reached stability, the number of particles corresponding to diameters of 10, 15, 20, 25, and 30 mm were 5,952, 3,289, 2,116, 1,067, and 638, respectively.

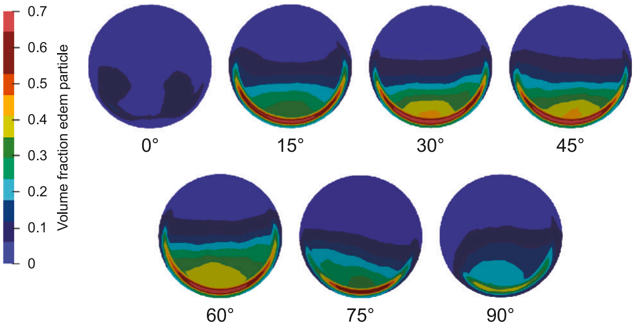

(a) u_f = 2 m/s

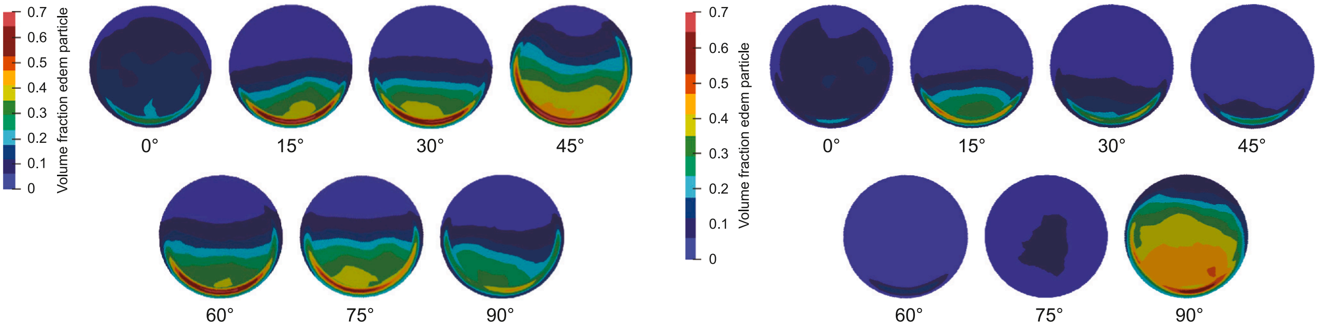

(b) u_f = 3 m/s **(c)** u_f = 4 m/s

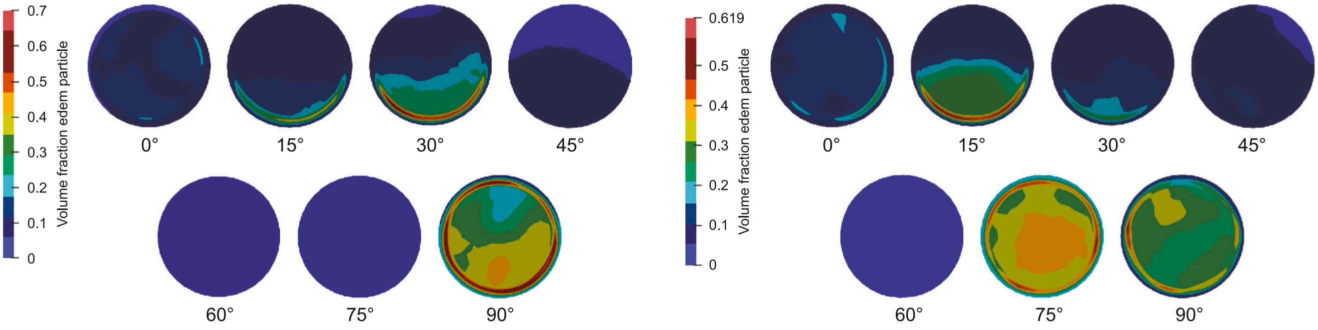

(d) u_f = 5 m/s **(e)** u_f = 6 m/s

Fig. 15. The particle volume fraction in seven sections at different conveying speeds.

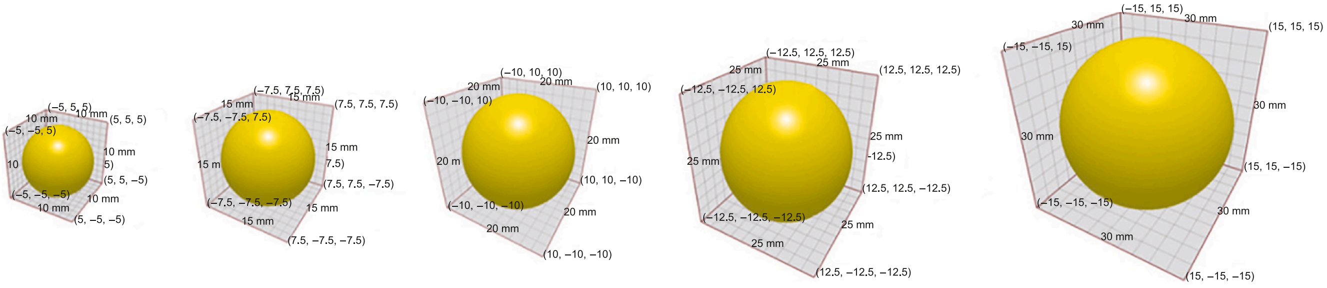

d_p = 10 mm d_p = 15 mm d_p = 20 mm d_p = 25 mm d_p = 30 mm

Fig. 16. Particle model under different particle sizes.

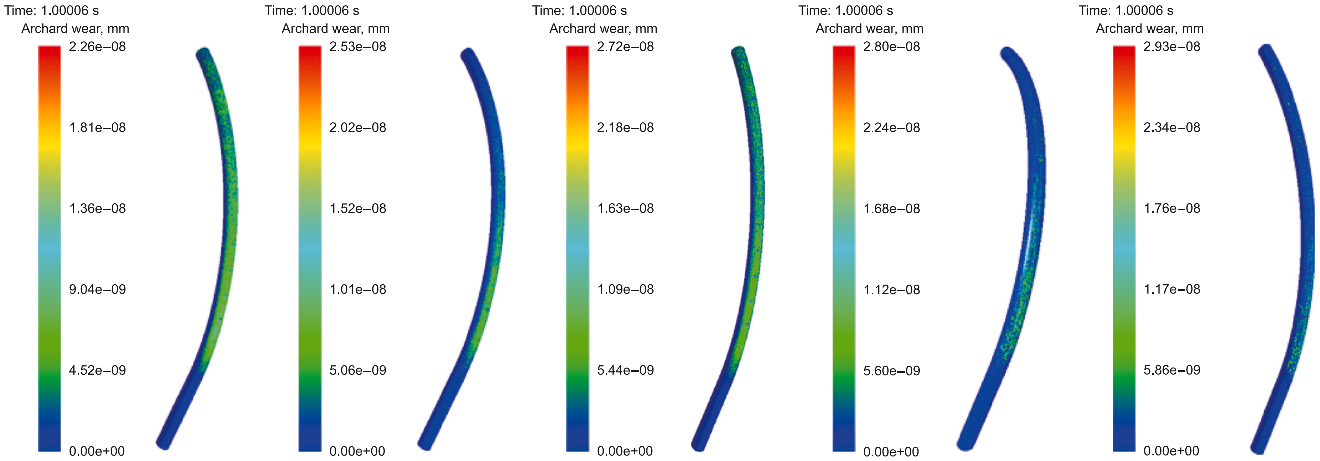

(a) d_p = 10 mm **(b)** d_p = 15 mm **(c)** d_p = 20 mm **(d)** d_p = 25 mm **(e)** d_p = 30 mm

Fig. 17. The wear cloud of the NMFP interior at five transport particle diameters.

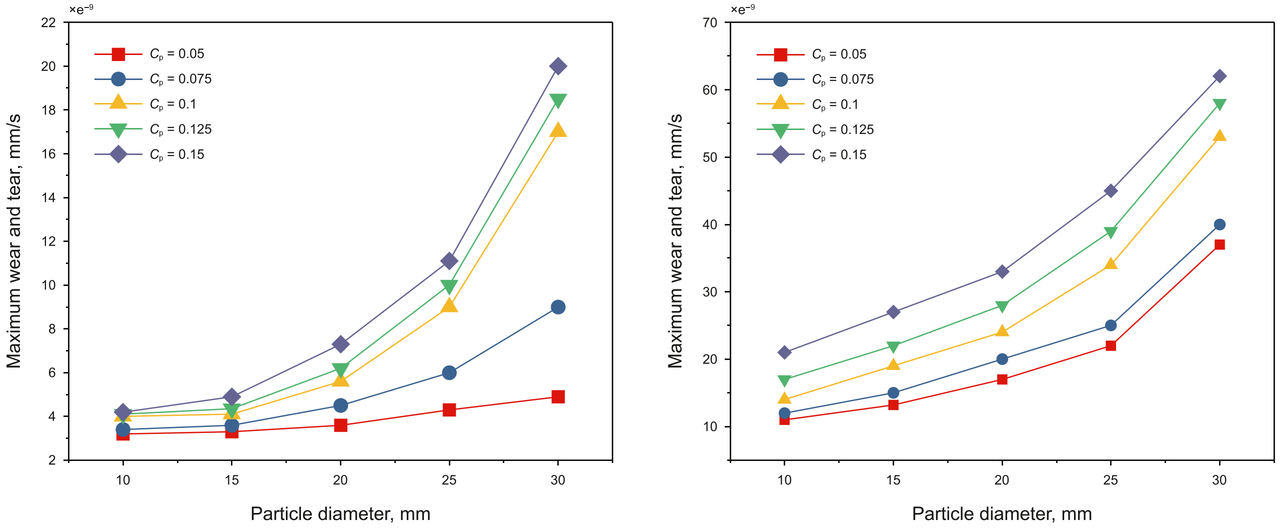

(a) Conveying speed of 3 m/s **(b)** Conveying speed of 5 m/s

Fig. 18. The maximum wear of the NMFP interior at different particle diameters.

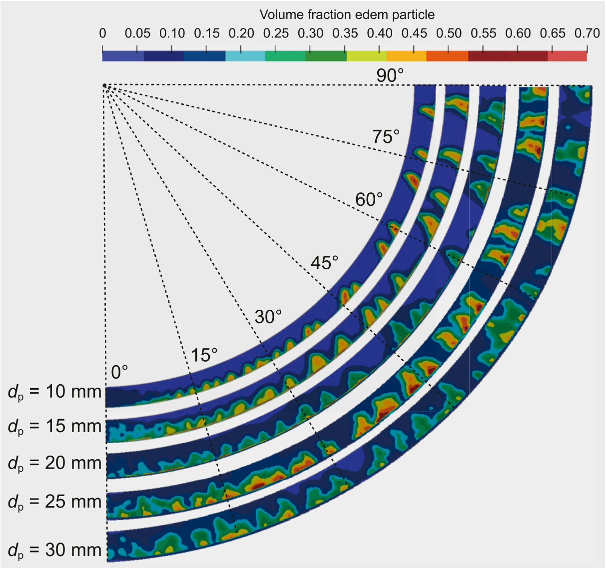

Fig. 19. The particle volume fraction in the flow field in different particle diameter conveying conditions.

Moreover, the ratio of the number of particles to the total number of collisions increased with larger particle diameters, significantly influencing the proportion of particle-wall collisions relative to the total collisions, which reached 45% at a particle size of 30 mm. Therefore, minimizing particle size is essential to reduce energy loss during the conveying process.

3.3. Conveying speed

During deep-sea mining NMFP hydraulic lifting, the diameters of the mineral particles are determined after fragmentation by the ore collection vehicle. The conveying speed is crucial for designing the lifting system. To mitigate hydraulic lifting challenges caused by low conveying velocity and avoid serious pipeline blockages, the conveying speed was adjusted to 2, 3, 4, 5, and 6 m/s at a particle diameter of 20 mm, while the feed concentration was set to 0.15. Fig. 12 shows the 1 s wear nephogram at different transmission speeds.

To establish the correlation between the maximum wear rate and the conveying speed, while minimizing the influence of particle diameter and feed concentration on the maximum wear value, the maximum wear variation of the bent NMFP was examined at five conveying speeds. The study considered particle

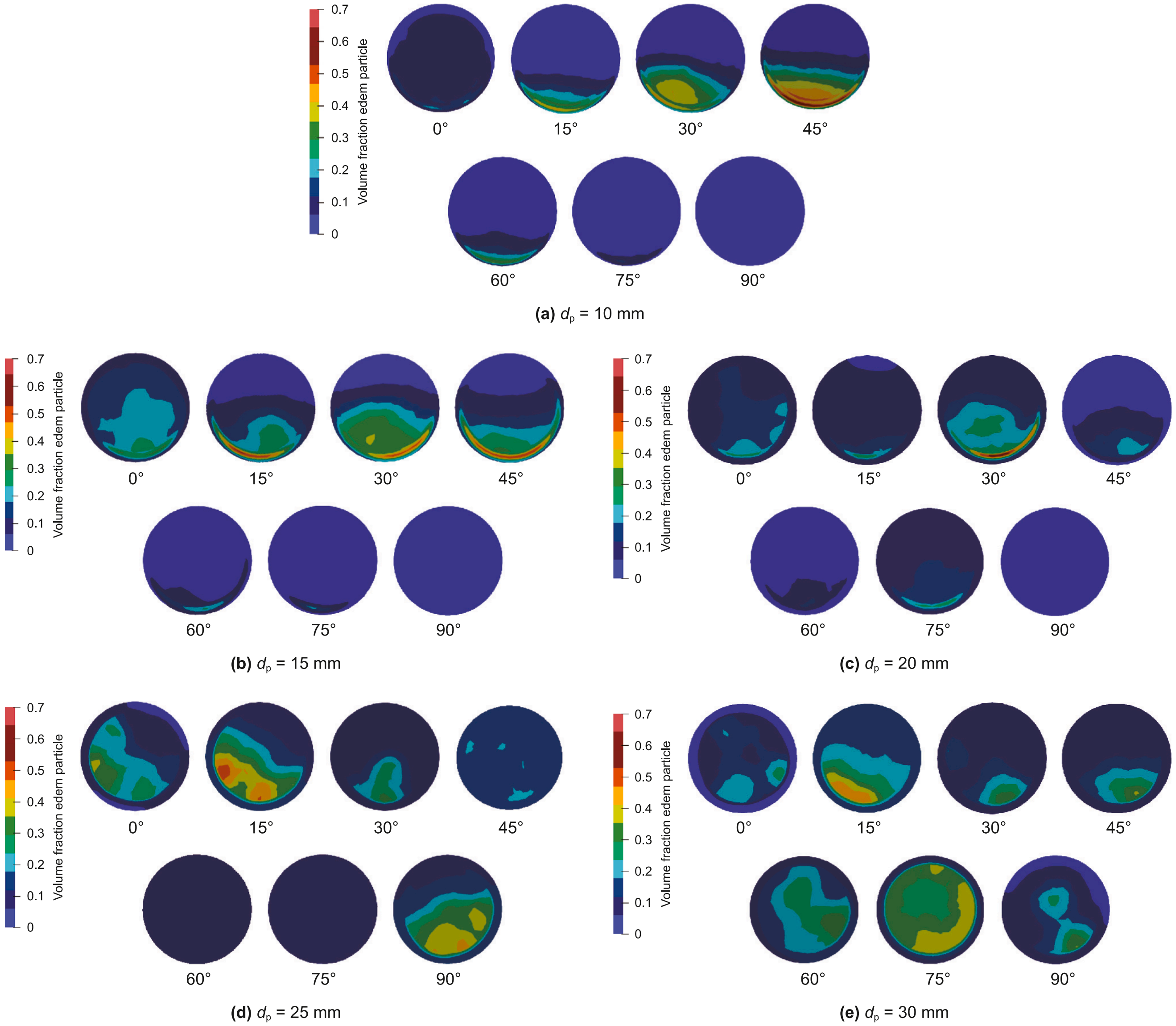

(a) d_p = 10 mm

(b) d_p = 15 mm

(c) d_p = 20 mm

(d) d_p = 25 mm

(e) d_p = 30 mm

Fig. 20. The particle volume fraction in seven sections at different particle diameters.

diameters of 20 and 30 mm, as well as feed concentrations of 0.05, 0.075, 0.1, 0.125 and 0.15 (Fig. 13).

At a maximum conveying speed of 6 m/s, a feed concentration of 0.15, and a particle diameter of 20 mm, the maximum annual wear of the corresponding NMFP liner was measured at 2.4219 mm/year. Consequently, an NMFP with an internal layer thickness of 10 mm has an operational lifespan of approximately 4.13 years. In contrast, at a particle diameter of 30 mm, the maximum annual wear of the NMFP interior was 2.7373 mm/year, resulting in a lifespan of about 3.65 years for an NMFP with the same internal thickness.

The study also analyzed the particle volume fraction distribution, pressure, and velocity within the flow field at five different conveying speeds. Additionally, the local concentration, local particle velocity, and slip velocity of the particles were investigated. Fig. 14 illustrates the particle volume fraction distribution across the five conveying speeds.

The particle volume fractions exhibited significant variations at different conveying speeds. Uniform particle transportation was observed along the outer wall of the flow field at conveying speeds of 2 and 3 m/s; however, uneven distribution occurred after the 30° section of the pipeline. As the particles were transported near the outer wall of the NMFP, the flow channel was obstructed by the transported particle flow. This obstruction led to an increase in fluid velocity in the interior, causing the particles in front to move rapidly upward and form clusters. A higher local concentration within the pipeline consequently elevated the risk of blockage.

Fig. 15 presents the particle volume fraction cloud diagram of the flow field across seven angled sections for each working condition. Particle transportation remained close to the outer wall of the NMFP at all conveying speeds. At lower feed concentrations, the particle volume concentration in the 45° section increased significantly. In some sections, particularly at higher conveying speeds, no particle volume fractions were detected. Conversely, the particles tended to distribute more evenly within the pipe upon exiting the curved sections.

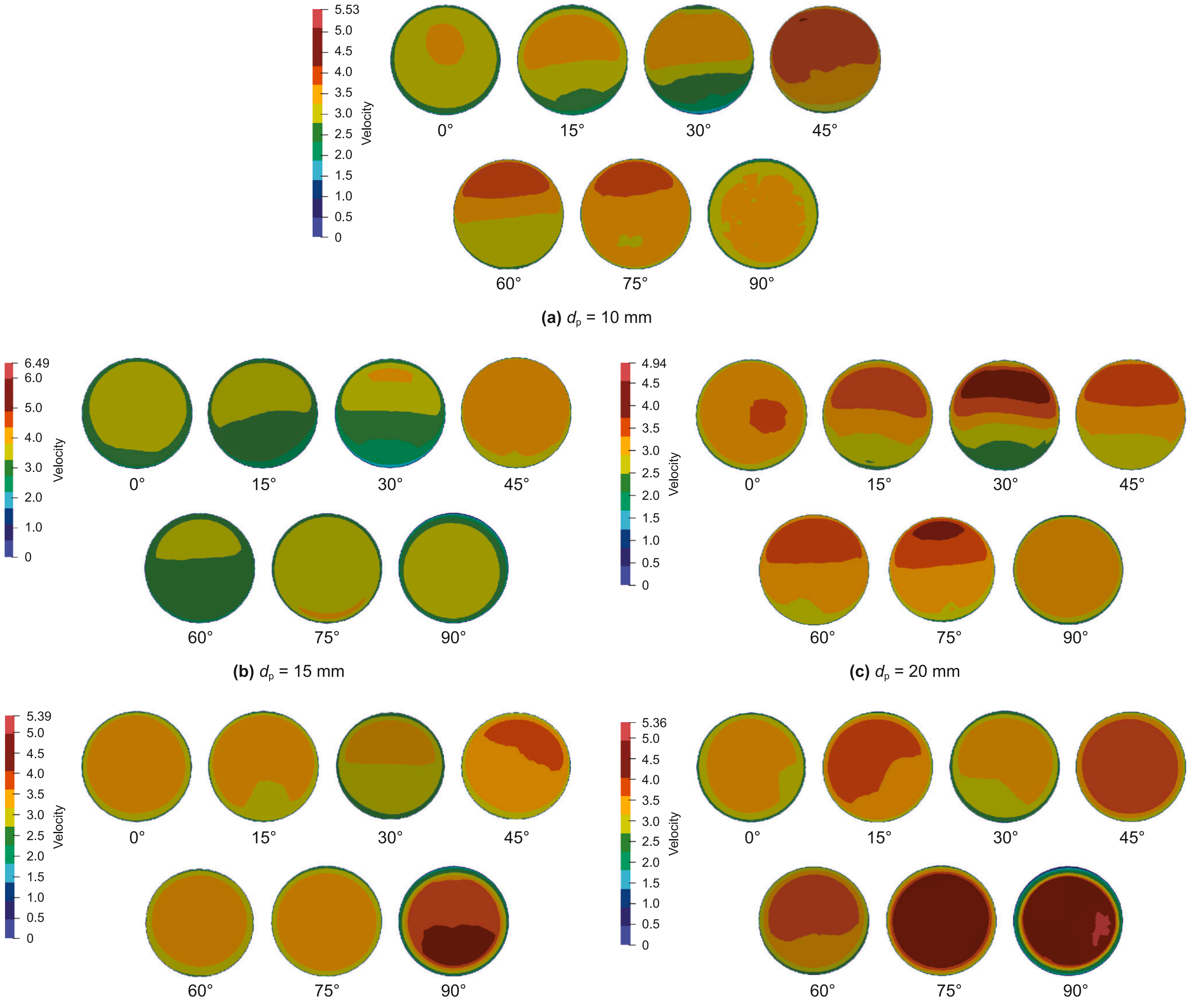

(a) d_p = 10 mm

(b) d_p = 15 mm

(c) d_p = 20 mm

(d) d_p = 25 mm

(e) d_p = 30 mm

Fig. 21. Flow field velocity of 7 sections under different particle diameters.

3.4. Particle diameter

The particle diameter is a critical parameter in the hydrodynamic lifting process of mineral particles, as particles of varying sizes exhibit distinctly different fluid dynamics within the flow field. To maintain consistency in transport conditions, the diameters of the transported particles were systematically adjusted. The selected particle diameters were 10, 15, 20, 25, and 30 (Fig. 16), as smaller-diameter mineral particles have a minimal impact on the overall flow field.

Fig. 17 presents the wear nephogram at different particle diameters, with a conveying speed of 3 m/s and a feeding concentration of 0.15. The degree of wear in the NMFP was found to be proportional to the particle diameter, with larger particles inducing greater wear. The maximum wear rates of the NMFP interior for particle sizes of 10, 15, 20, 25, and 30 mm were measured at 2.26×10^{-8}, 2.53×10^{-8}, 2.70×10^{-8}, 2.80×10^{-8}, and 2.93×10^{-8} mm/s, respectively (see Fig. 17).

As shown in Fig. 18, to determine the correlation between the maximum wear rate and particle diameter, while minimizing the influence of conveying speed and feed concentration on maximum wear, the variation in maximum wear within the internal layer of the NMFP was investigated at conveying speeds of 3 and 5 m/s. The study employed feed concentrations of 0.05, 0.075, 0.1, 0.125, and 0.15, along with five different particle sizes.

At a maximum particle diameter, feed concentration, and a conveying speed of 3 m/s, the highest annual wear on the interior of the NMFP is 0.631 mm/year. Consequently, an NMFP with an internal thickness of 10 mm would have a service life of approximately 15.85 years. At a conveying speed of 5 m/s, the maximum annual wear increased to 1.955 mm/year, reducing the service life of the NMFP to about 5.12 years.

Fig. 19 illustrates the volume fraction distribution of particles with five different diameters within the NMFP, revealing significant variations. Particles with a 10 mm diameter were concentrated near the outer wall. As particle diameter increased, their distribution became more uniform across the radial direction. However, due to the influence of centrifugal force, the highest volume fraction remained near the outer wall.

Fig. 20 shows the particle volume fraction cloud diagram in seven angular sections of the flow field under varying particle diameters. Prior to the 45° section, particle transport occurred predominantly near the outer wall of the NMFP. For particle diameters of 10 mm and 15 mm, the particle volume fractions in the radial position increased progressively before reaching the 45° section. After the 45° section, certain pipe segments exhibited areas with no particle volume fraction, indicating the formation of particle clusters. For larger diameters (20, 25, and 30 mm), the particles were more evenly distributed, with the highest particle volume fraction concentrated along the outer wall.

The velocity contour maps of the flow field at the cross-sections of seven angles during the conveying process with different particle diameters are obtained and presented in Fig. 21. As can be observed from the figure, when the particle diameters are $d_\mathrm{p} = 10$, 15, and 20 mm, the velocity distribution of the flow field during particle conveying shows a stratified phenomenon. The regions with relatively higher velocities are located at the inner wall surface of the flexible pipe. Due to the presence of particles, a “low-velocity zone” is formed at the outer wall surface. When the particle diameters increase to 25 mm and 30 mm, the velocity regions of the flow field tend to be stable at the positions of the seven cross-sections, and the maximum velocity value appears at the cross-section of 90°.

4. Conclusion

In this paper, the wear characteristics in the NMFP interior during hydraulic lifting are analyzed using the CFD-DEM approach, incorporating principles of fluid mechanics, particle collision models, and the Archard wear model. The results show that particle velocities increase sharply upon entering the flow field due to the influence of the conveying fluid, followed by fluctuations around the average velocity during transport. Lower conveying speeds lead to localized particle concentration and aggregation, which stabilize over time, with higher speeds accelerating this stabilization. The maximum wear rate of the NMFP increases with conveying speed, particle diameter, and feed concentration. Specifically, when the conveying speed is 6 m/s, the feed concentration is 0.15, and the particle diameter is 30 mm, the maximum annual wear rate reaches 2.7373 mm. This indicates that an NMFP with an internal thickness of 10 mm can be utilized for 3.65 years. Furthermore, particle collisions are correlated with energy loss. The ratio of particle-wall collisions to the total number of collisions, together with the proportion of kinetic energy, increases with the conveying speed and particle size. But this article primarily explores the patterns of pipe wear and optimal conveying conditions under specific particle diameters and conveying speeds. In the future, the influence of multi-factor coupling effect on flexible pipe wear should be further considered to find out the possible maximum influencing factors.

CRediT authorship contribution statement

Ying-Ying Wang: Writing – review & editing, Writing – original draft, Visualization, Validation, Methodology, Funding acquisition. **Yun-Di Liu:** Writing – review & editing, Writing – original draft, Visualization, Validation, Supervision, Software, Resources, Methodology, Formal analysis. **Ze-Qing Lin:** Writing – review & editing. **Hai-Bo Sun:** Writing – review & editing, Writing – original draft. **Zhuo Cheng:** Writing – review & editing, Writing – original draft, Visualization, Validation. **Ke Wang:** Writing – review & editing, Visualization, Validation. **Ding-Wen Huang:** Writing – original draft.

Declaration of interest statement

The authors declare that we have no conflict of interest or personal relationships that could have appeared to influence the work reported in this paper.

Acknowledgments

The authors thank the support provided by: “The Key Research and Development Program of Shandong Province, China (Grant No. 2024CXGC010802)”, the “Taishan Industial Experts Program”, the “Integrated Design Theory and Risk Prevention & Control Method of Mining and Transportation System for Deep-sea Poly Metallic Nodules (Grant No. 52394255)”, and the “National Key Research and Development Program of China: Design and Key Technology Research of Non-metallic Flexible Pipes for Deep Sea Mining (Grant No. 2022YFC2803701)”.

References

Araoye, A.A., Badr, H.M., Ahmed, W.H., Habib, M.A., Alsarkhi, A., 2017. Erosion of a multistage orifice due to liquid-solid flow. Wear 390–391, 270–280.

Blanchard, D.J., Greeith, P., Rabinowicz, E., 1984. Erosion of a pipe bend by solid particles entrained in water. J. Eng. Ind. 106 (3), 213. https://doi.org/10.1115/1.3185935.

Bellman, R., Levy, A., 1981. Erosion mechanism in ductile metals. Wear 70, 1–28. https://doi.org/10.1177/1687814019892136.

Badur, J., Karcz, M., Lemański, M., 2011. On the mass and momentum transport in the navier−stokes slip layer. Microfluid. Nanofluidics 11, 439–449. https://doi.org/10.1007/s10404-011-0809-2.

Chen, X., Mclaury, B.S., Shirazi, S.A., 2006. Numerical and experimental investigation of the relative erosion severity between plugged tees and elbows in dilute gas/solid two-phase flow. Wear 261 (7/8), 715–729. https://doi.org/10.1016/j.wear.2006.01.022.

Chen, L.Y., Duan, Y.F., Liu, M., Zhao, C.S., 2010. Slip flow of coal water slurries in pipelines. Fuel 89, 1119–1126. https://doi.org/10.1016/j.fuel.2009.09.016.

Choi, C.Y., Yoon, H.S., Ha, M.Y., 2010. Flow around a freely falling square shape particle in a channel using direct-forcing fictitious domain method. J. Mech. Sci. Technol. 24 (7), 1441–1449. https://doi.org/10.1007/s12206-010-0422-4.

Choi, C.Y., Yoon, H.S., Ha, M.Y., 2013. Flow and motion characteristics of a freely falling square particle in a channel. Comput. Fluid 79, 1–12. https://doi.org/10.1016/j.compfluid.2013.02.019.

Chen, L., Zhu, H.Y., Cui, H.H., 2017. A study of the Brownian motion of the non-spherical microparticles on fluctuating lattice Boltzmann method. Microfluid. Nanofluidics 21, 54. https://doi.org/10.1007/s10404-017-1880-0.

Darihaki, F., Zhang, J., Vieira, R.E., Shirazi, S.A., 2021. The near-wall treatment for solid particle erosion calculations with CFD under gas and liquid flow conditions in elbows. Adv. Powder Technol. 32 (5), 1663–1676. https://doi.org/10.1016/j.apt.2021.03.020.

Frawley, P., Corish, J., Niven, A., Geron, M., 2009. Combination of CFD and DOE to analyse solid particle erosion in elbows. Int. J. Comput. Fluid Dynam. 23 (5), 411–426. https://doi.org/10.1080/10618560902919279.

Glasby, G.P., Li, J., Sun, Z.L., 2015. Deep-Sea nodules and Co-rich Mn crusts. Mar. Georesour. Geotechnol. 33 (1), 72–78. https://doi.org/10.1080/1064119X.2013.784838.

Hannington, M., Petersen, S., Krätschell, A., 2017. Subsea mining moves closer to shore. Nat. Geosci. 10, 158. https://doi.org/10.1038/ngeo2897.

Leng, D.X., Shao, S., Xie, Y.C., 2021. A brief review of recent progress on deep sea mining vehicle. Ocean Eng. 228, 108565. https://doi.org/10.1016/j.oceaneng.2020.108565.

Lu, Y., Glass, D.H., Easson, W.J., 2009. An investigation of particle behavior in gas-solid horizontal pipe flow by an extended LDA technique. Fuel 88, 2520–2531. https://doi.org/10.1016/j.fuel.2009.02.038.

Liu, X.L., Yue, S., Lu, L.Y., Gao, W., Li, J.L., 2018. Numerical simulations of a gas-solid two-phase impinging stream reactor with dynamic inlet flow. Energies 11, 1913. https://doi.org/10.3390/en11071913.

Li, Y., Cao, G.P., Xie, C.J., 2021. Research on the wear characteristics of a Bend pipe with a bump based on the coupled CFD-DEM. J. Mar. Sci. Eng. 672 (9). https://doi.org/10.3390/jmse9060672.

Liu, X.F., Zhou, J.F., Gao, S.Q., 2022. Study on the impact wear characteristics of catalyst particles at 90° elbow via CFD-DEM coupling method. J. Appl. Fluid Mech. 15 (1), 221–230. https://doi.org/10.47176/jafm.15.01.32536.

Lin, C., Xu, Q.C., Han, L.X., Li, G., He, H., Zhou, H.L., She, J.P., 2024. Fracture sealing performance of granular lost circulation materials at elevated temperature: a theoretical and coupled CFD-DEM simulation study. Pet. Sci. 21, 567–581. https://doi.org/10.1016/j.petsci.2023.10.002.

Ran, J.Y., Zhang, L., Tang, Q., Xin, M.D., 2006. Numerical simulation of the particle motion characteristics in boundary layer of gas-solid rotary flow. ASME. J. Fluids Eng. 128 (3), 596–601. https://doi.org/10.1115/1.2175166.

Shen, Z.J., Li, R.N., Han, W., Zhao, W.J., Wang, X.H., 2016. The research on particle trajectory of solid-liquid two-phase flow and erosion predicting in screw centrifugal pump. IOP Conf. Ser. Mater. Sci. Eng. 129, 012052. https://doi.org/10.1088/1757-899X/129/1/012052.

Singh, J., Kumar, S., Singh, J.P., Kumar, P., Mohapatra, S.K., 2019. CFD modeling of erosion wear in pipe bend for the flow of bottom ash suspension. Part. Sci. Technol. 37 (3), 275–285. https://doi.org/10.1080/02726351.2017.1364816.

Sun, H.B., Wang, Y.Y., Jia, L.S., Lin, Z.Q., Yu, H., 2024. Theoretical and numerical methods for predicting the structural stiffness of unbonded flexible Pipe for deep-sea mining under axial tension and internal pressure. Ocean Eng. 310, 118672. https://doi.org/10.1016/j.oceaneng.2024.118672.

Sun, H.B., Wang, Y.Y., Lin, Z.Q., Dong, L.L., Liu, G., Yu, H., 2026. A novel analytical model for the failure envelope of composite pipes under axisymmetric loading. Mar. Struct. 105, 103908. https://doi.org/10.1016/j.marstruc.2025.103908.

Takano, S., Sato, S., Terao, T., Masanobu, S., Kawano, S., 2022. Study on pipe wear based on large Scale experiment and scale effect for deep sea mining. J. Offshore Mech. Arctic Eng. 144, 11803–11805. https://doi.org/10.1115/1.4052178.

Van Wijk, J., Talmon, A., Van Rhee, C., 2016. Stability of vertical hydraulic transport processes for deep ocean mining: an experimental study. Ocean Eng. 125, 203–213. https://doi.org/10.1016/j.oceaneng.2016.08.018.

Van Wijk, J., Van Rhee, C., Talmon, A., 2014. Wall friction of coarse grained sediment plugs transported in a waterflow through a vertical pipe. Ocean Eng. 79, 50–57. https://doi.org/10.1016/j.oceaneng.2014.01.010.

Wu, J.D., Yuan, X.Y., Fan, Y.G., Wang, X.D., 2012. Modeling and experimental verification of solid-liquid two-phase flow long-distance pipeline friction drag loss based on LS-SVM. Adv. Mater. Res. 485, 548–553. https://doi.org/10.4028/www.scientific.net/AMR.485.548.

Wang, K., Liu, H.Y., Wang, L.K., 2024. Effect of particle size on vortex structure and erosion behavior of semi-open centrifugal pump. Energy 293, 130576. https://doi.org/10.1016/j.energy.2024.130576.

Wang, Y.Y., Cheng, Z., Yin, B., Liu, B.L., Wang, K., 2024. Simulation of special-shaped graded particulate hydraulic transport in deep-sea mining scenarios. Powder Technol. 448, 120344. https://doi.org/10.1016/j.powtec.2024.120344.

Yan, F., Tu, P.P., Li, X., Chen, Y., Zheng, Y., Zhu, R., 2021. Dynamic analysis of particles in vertical curved 90° bends of a horizontal-vertical pneumatic conveying system based on POD and wavelet transform. Adv. Powder Technol. 32, 1399–1409. https://doi.org/10.1016/j.apt.2021.03.005.

Yang, H.L., Fan, M.Q., Liu, A.R., Dong, L.P., 2015. General formulas for drag coefficient and settling velocity of sphere based on theoretical law. Int. J. Min. Sci. Technol. 25 (2), 219–223. https://doi.org/10.1016/j.ijmst.2015.02.009.

Yao, L.M., Liu, Y.X., Xiao, Z.M., 2023. An algorithm combining sedimentation experiments for pipe erosion investigation. Energy 270, 126891. https://doi.org/10.1016/j.energy.2023.126891.

Yin, B., Lou, Y.S., Liu, S.Y., Zhang, Y., 2025. Mechanism of proppant transport and deposition in rough intersecting fractures after offshore fracturing. Pet. Sci. 22, 1270–1288. https://doi.org/10.1016/j.petsci.2025.01.008.

Yang, N., Chen, G.G., Tang, D.S., Jin, X., Xiao, H., 2011. Behavior of Single Particle and Group Particles in Vertical Lifting Pipe in China. the Ninth ISOPE Ocean Mining Symposium, Maui, Hawaii, USA. https://doi.org/10.4043/23003-MS.

Zhao, Y.L., Tang, C.Y., Yao, J., 2020. Investigation of erosion behavior of 304 stainless steel under solid–liquid jet flow impinging at 30°. Pet. Sci. 17, 1135–1150. https://doi.org/10.1007/s12182-020-00473-7.

Zhang, J., Mclaury, B.S., Shirazi, S.A., 2015. Modeling sand fines erosion in elbows mounted in series. Wear 402–403, 196–206. https://doi.org/10.1016/j.wear.2018.02.009.